

Article

Effects of Porosity, Heat Input and Post-Weld Heat Treatment on the Microstructure and Mechanical Properties of TIG Welded Joints of AA6082-T6

Bo Wang ¹, Songbai Xue ^{1,*}, Chaoli Ma ¹, Jianxin Wang ² and Zhongqiang Lin ³

¹ College of Materials Science and Technology, Nanjing University of Aeronautics and Astronautics, Nanjing 210016, China; wangbo4175@126.com (B.W.); machaoli006@163.com (C.M.)

² Jiangsu Provincial Key Laboratory of Advanced Welding Technology, Jiangsu University of Science and Technology, Zhenjiang 212003, China; wangjx_just@126.com

³ Zhejiang Yuguang Aluminum Material Co., Ltd., Jinhua 321200, China; linzhongqiang666@163.com

* Correspondence: xuesb@nuaa.edu.cn; Tel.: +86-025-8489-6070

Received: 21 September 2017; Accepted: 24 October 2017; Published: 1 November 2017

Abstract: Various heat input conditions and post-weld heat treatments were adopted to investigate the microstructure evolution and mechanical properties of tungsten inert gas (TIG) welded joints of AA6082-T6 with porosity defects. The results show that the fracture location is uncertain when an as-welded joint has porosities in the weld zone (WZ), and overaging in the heat-affected zone (HAZ) at the same time. When the fracture of the as-welded joint occurs in the HAZ, the total heat input has a linear relation with the tensile strength of the joint. An excess heat input induces the overgrowth of Mg₂Si precipitates in HAZ and the coarsening of α -Al grains in WZ, resulting in a decrease in the microhardness of the corresponding areas. After artificial aging treatment, the tensile strength of the welded joint is increased by approximately 9–13% as compared to that of as-welded joint, and fracture also occurs in HAZ. In contrast, for solution treated and artificial aging treated joint, fracture occurs suddenly at the rising phase of the tensile curve due to porosity defects throughout the weld metal. Furthermore, the eutectic Si particles of WZ coarsen and spheroidize after solution treatment and artificial aging treatment, due to the diffusion of Si to the surface of the original Si phases when soaking at high temperature.

Keywords: aluminum alloy; welding; weld porosity; heat input; heat treatment; microstructure; mechanical properties

1. Introduction

The 6XXX series aluminum alloys have been used extensively in the aeronautical, maritime, and ground transportation industries, due to their moderate strength, outstanding weldability, and excellent corrosion resistance [1]. Moreover, the mechanical properties of such alloys can even be enhanced by solution treatment and artificial or natural aging. Due to these properties, the alloys have served as one of the most important aluminum alloy structural materials in the field of welding. Thus, the welding technology of 6XXX series aluminum alloys is a key process that affects the wide application of the alloys. For example, welding 6XXX aluminum alloys by tungsten inert gas (TIG) arc welding is characterized by stable arc, no spatter, and good weld formation. However, due to the intrinsic problem of overaging in heat-affected zone (HAZ) [2] and hydrogen porosity in aluminum welding [3], it remains a great challenge for designers and technologists to join 6XXX aluminum alloys by fusion welding.

After welding, an overaging phenomenon, imposed by the weld thermal cycle, occurs at the HAZ, which decreases the mechanical resistance of the welded joint (tensile strength and hardness).

The tensile properties and microhardness evolution of the heat-treatable aluminum alloy welds have been studied by several authors [4–6]. Ambriz et al. [7] studied the Vickers microhardness distribution of 6061-T6 joints welded using a modified indirect electric arc (MIEA) technique to determine the different zones of the joints. They found a soft zone in the HAZ with hardness values of approximately 61.2 HV and a yield strength decrement of approximately 50%, with respect to the base metal.

In addition to overaging of the HAZ for heat-treatable aluminum joints, defects in the weld metal are also important for performance reduction as well as failure mode. The high coefficient of thermal expansion of aluminum, solidification shrinkage, and high solubility of hydrogen during its molten state create associated weld defects during fusion welding of aluminum alloys [8]. As a consequence, weld defects are quite common and can be in the form of surface or subsurface cracks, undercut, porosity, or subsurface inclusions. Porosity and other defects can influence the mechanical properties negatively, which are very common in high melting/cooling processing methods, such as welding or laser-based ones [9,10]. Thus, an important decision related to its structural integrity must be made regarding weld defects and their effects on the strength of welded components. Only a limited number of studies have been reported in the literature on the effects of weld defects on the mechanical performances of heat-treatable aluminum alloy joints [8,11–13]. Rudy and Rupert [11] and Gou et al. [12] studied the effect of porosity on AA2XXX and AA7XXX welded joints, respectively. Morton [13] showed a linear relationship between fracture strength and projected defect areas of TIG welded AA2XXX aluminum alloy. However, no comprehensive data exist on weld porosities and their effects on a TIG welded joint of AA6082 aluminum alloy. A comparison between the effect of porosities in weld zone (WZ) and the effect of overaging in HAZ is required for predicating and evaluating the mechanical properties of a TIG welded joint of AA6XXX.

Due to the welding heat, the materials in the HAZ and WZ become softer and more susceptible to failure [14]. Different post-weld heat treatment (PWHT) techniques are usually applied to improve the mechanical performances of welded joints of heat-treatable aluminum alloys. A number of research studies have investigated the application of PWHT to different aluminum alloy welded joints using various welding processes [15–18]. Balasubramanian et al. [19] researched the effect of pulsed current and PWHT on the tensile properties of TIG welded and metal inert gas (MIG) welded high-strength aluminum alloys; they noted that more precipitates were formed after a soaking period of 24 h at 125 °C, and their uniform distribution led to a higher strength and hardness. Pérez et al. [20] reported that the microstructural damage produced by the weld thermal cycle in the HAZ can be reverted by a PWHT consisting of solubilization and artificial aging (T6). However, very few investigations have shown the effect of PWHT on fusion welded AA6XXX aluminum alloys with porosity defects [8].

The above-mentioned investigations focused mainly on the influence of PWHT on the microstructures and the mechanical properties of welded joints without weld defects. However, the influence of welding parameters (in particular, heat input) and PWHT on the microstructures and mechanical properties of TIG welded joints of 6082-T6 aluminum alloy with porosities is still an open question. Hence, in this article, an attempt has been made to examine the integrated effects of heat input, PWHT, and porosities on the mechanical properties of multipass welded joints of AA6082. Moreover, the relationship between redefined heat input and tensile strength of the 6082 weld specimen is discussed in detail.

2. Materials and Methods

2.1. Materials and Welding Process

6082-T6 aluminum plates (base materials) with a thickness of 12 mm and ER4043 aluminum welding rods with a diameter of 3.2 mm were used in the welding process. Their chemical compositions (in weight percentage) are shown in Table 1. The welding direction was placed parallel to the rolling direction of the base materials, and a schematic diagram of the multipass weld bead is shown in Figure 1. TIG welding in the vertical position, which was exerted by an AOTAI WSME-500 welder

(Aotai Electric, Jinan, China), was employed. Argon with a purity of 99.99% was used as the shielding gas. Each plate was cleaned with acetone and steel brush to remove the oxide layer and other contaminants from the surface of the samples before welding. In addition, the plates were preheated due to the high thermal conductivity of the aluminum alloy (the thermal conductivity of 6082-T6 alloy is $180 \text{ W} \cdot (\text{m} \cdot \text{K})^{-1}$). A matrix of welding parameters providing different heat inputs is presented in Table 2. All of the welds performed were visually and were nondestructively inspected for possible defects using an X-ray film photographic inspection method. The radiography test was performed by using an XY-2512 X-ray flaw detector (Zhongyi Electronic, Dandong, China). The radiographs of these welds were obtained using X-rays at 68 kV and 15 mA and were used to assess the quality levels for imperfections of these welded joints according to DIN EN ISO 10042:2006.

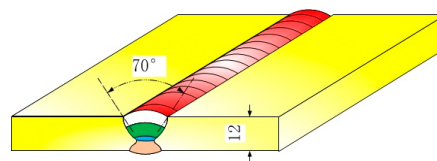


Figure 1. Schematic diagram of the multipass weld bead (mm).

Table 1. Chemical composition (wt. %) of base metal and welding rod.

| Materials | Si | Fe | Cu | Mn | Mg | Ti | Al |
|-----------|------|-------|-------|------|------|-------|-----------|
| 6082 | 0.83 | 0.296 | 0.059 | 0.55 | 1.14 | 0.018 | Remainder |
| 4043 | 5.05 | 0.110 | 0.024 | - | - | 0.034 | Remainder |

Table 2. Welding parameters.

| Plate No. | Preheat Temperature/ $^{\circ}\text{C}$ | Interpass Temperature/ $^{\circ}\text{C}$ | Current/A | Gas Flow L/min | Weld Pass Face/Back |
|-----------|---|---|-----------|----------------|---------------------|
| 1 | 50 | 60 | 225 | 16 | 5/2 |
| 2 | 50 | 60 | 225 | 16 | 5/1 |
| 3 | 100 | 110 | 250 | 16 | 8/2 |
| 4 | 100 | 95 | 260 | 16 | 3/2 |
| 5 | 102 | 88 | 280 | 16 | 5/1 |
| 6 | 100 | 100 | 288 | 16 | 3/2 |
| 7 | 65 | 75 | 303 | 16 | 4/2 |
| 8 | 90 | 86 | 320 | 16 | 3/2 |

2.2. PWHT (Post-Weld Heat Treatment) and Performance Tests

The specific parameters of different PWHTs are shown in Table 3. Each welded plate was divided into three identical welded samples. These welded samples were treated with different PWHTs and were divided into three types: AW, AG, and SAG.

Table 3. Post-weld heat treatment (PWHT) parameters.

| Abbreviation | PWHT | Specific Process Parameters |
|--------------|---|---|
| AW | As-welded | - |
| AG | Artificial aging treatment | $160 \text{ }^{\circ}\text{C} \times 18 \text{ h}$ |
| SAG | Solution treatment + artificial aging treatment | $530 \text{ }^{\circ}\text{C} \times 30 \text{ min} + 160 \text{ }^{\circ}\text{C} \times 18 \text{ h}$ |

Full-size transverse tensile specimens were machined from the welded plates according to ASTM E8 so that the weld was centered in the gauge section, and the loading axis was normal to the welding direction. To avoid the effect of weld profile on the stress concentration during the tensile test, the weld

reinforcement was grinded with a polisher (Fujian Hitachi Koki Co., Ltd., Fuzhou, China) prior to being tested. Tensile tests were performed on a WAW-300B testing machine (Zhejiang Jingyuan Mechanical Equipment Co., Ltd., Jinhua, China) operating at room temperature and the average value of the test results were calculated. In order to ensure the accuracy of the results, three tensile specimens under the same heat treatment conditions were prepared. The Vicker's hardness measurements were conducted with 1.0 mm spacing on the cross section of these welded joints using an HXS-1000A microhardness tester (Teshi Testing Technology (Shanghai) Co., Ltd., Shanghai, China), under a load of 200 g for 15 s. Each point was tested three times and the average value of the test results were calculated. The specimens from the butt-welded joints were suitably sectioned, mounted, mechanically polished, and etched. The etchant was 0.5% HF solution. For microstructural observations and analyses of fracture surfaces, the specimens were observed using a TV-400D optical microscopy (Shanghai Tuanjie Instrument Manufacturing Co., Ltd., Shanghai, China) and a ZEISS Σ IGMA field-emission scanning electron microscope coupled to an energy dispersion X-ray (FE-SEM/EDX; Carl Zeiss, Oberkochen, Germany). Furthermore, the chemical compositions of the different areas in the welded joint were measured using a SPECTRO[®] MAXx04D spectrometer (SPECTRO Analytical Instruments GmbH, Kleve, Germany).

3. Results and Discussion

3.1. Results of Nondestructive Testing (NDT) and Calculation of Total Heat Input (TQ)

According to standard ISO 10042:2006, the weld percent porosity (WPP) is quantified by the ratio of the porosity area to the weld projected area [21]. All of the welds were detected as unqualified by the NDT (Nondestructive testing) method and assessed as the last grade. Excess porosities were found in all of these welds. In addition, the weld of sample No. 5 was detected to have a weld line defect, which was due to the lack of penetration with a length of 180 mm along the welding direction. The NDT photographs of representative welded joints (samples No. 4 and 6) containing varied porosities are shown in Figure 2. The cross-sectional macrostructures of representative welded joints (samples No. 5 and 6) are shown in Figure 3.

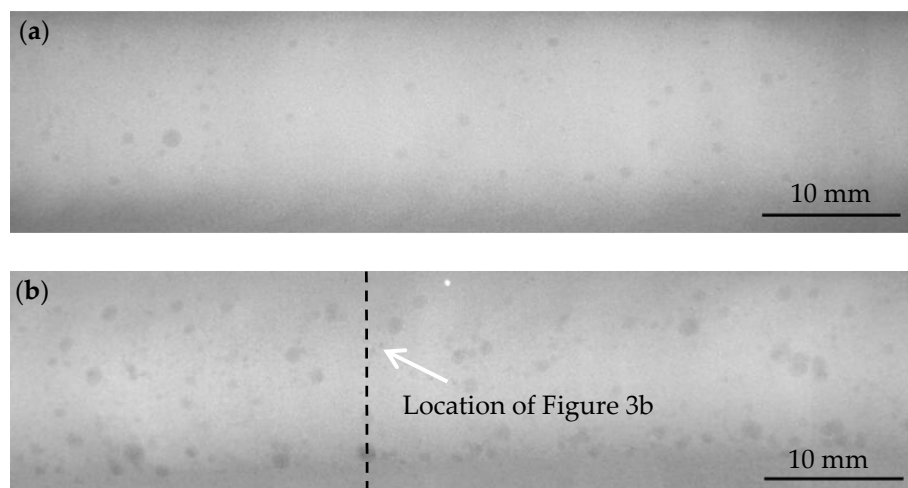


Figure 2. Nondestructive testing (NDT) photographs of representative welded joints: (a) sample No. 4; (b) sample No. 6.

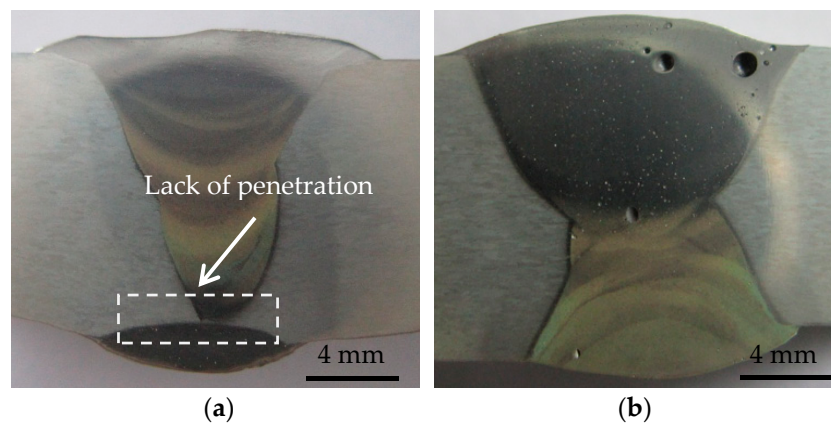


Figure 3. Cross-sectional macrostructures of representative welded joints: (a) sample No. 5; (b) sample No. 6.

The heat input value Q (kJ/mm) may be calculated as follows according to the European Standard EN 1011-1:

$$Q = k \times \frac{U \times I}{v} \times 10^{-3} \quad (1)$$

where U is the welding voltage, v is the welding speed, I is the welding current, and k is the efficiency of TIG welding ($k = 0.6$, corresponding to the welding process No. 141).

Multipass welding is essential for producing a TIG welded joint of AA6082-T6 due to the middle thickness of the plate. The welding speed v in one weld pass may differ from another during manual TIG welding process, so the Q of each weld pass is also different. To study the accurate relationship between heat input and tensile strength of a TIG welded joint, the total heat input value TQ is first proposed as follows:

$$\begin{aligned} TQ &= Q_1 \times S_1 + Q_2 \times S_2 + \dots + Q_n \times S_n + \dots + Q_m \times S_m \\ &= \sum_{n=1}^m (Q_n \times S_n) \end{aligned} \quad (2)$$

where S is the measured length of each weld pass, subscript n is the number of each weld pass, and subscript m is the total number of all the weld passes.

The tensile strength $R_m(w)$ of the welded test specimen in the post-welded condition shall satisfy the following requirement according to ISO 15614-2:2005(E):

$$R_m(w) = R_m(pm) \times T \quad (3)$$

where $R_m(pm)$ is the specified minimum tensile strength of the parent material required in the relevant standard, and for AA6082-T6 plate with a thickness of 12 mm, $R_m(pm) = 300$ MPa according to DIN EN 485-2:2013. T is the joint efficiency factor, and $T \geq 0.6$ is determined as qualified according to ISO 15614-2.

According to Equations (1)–(3) and the standard ISO 10042:2006, the test results including tensile strength $R_m(w)$, yield strength R_p , and elongation A of the as-welded joints and the calculation results including T and TQ , conventional heat input Q and weld percent porosity WPP are listed in Table 4.

Table 4. Tensile properties of butt welded joints as a result of heat input.

| Plate No. | $R_m(w)/MPa$ | R_p/MPa | $A/\%$ | Fracture Location | $T/\%$ | TQ/kJ | Q kJ/mm | $WPP/\%$ |
|----------------|--------------|-----------|--------|-------------------|--------|---------|-----------|----------|
| 1 | 141 | - | - | HAZ | 47 | 7126.9 | 2.91 | 5.34 |
| 2 | 150 | 112 | 6.9 | HAZ | 50 | 5791.8 | 2.76 | 6.22 |
| 3 | 186 | 179 | 5 | HAZ | 62 | 4011 | 1.15 | 5.10 |
| 4 | 176 | 145 | 9.7 | HAZ | 58.7 | 4878.3 | 2.79 | 2.58 |
| 5 ¹ | 173.5 | 149 | 4 | WZ | 57.8 | 4834.8 | 2.30 | 4.36 |
| 6 | 185 | 177 | 4.2 | WZ | 61.7 | 3370.5 | 1.93 | 8.50 |
| 7 | 193 | 157 | 7.1 | HAZ | 64.3 | 3784.4 | 1.80 | 3.46 |
| 8 | 191 | 160 | 6.5 | HAZ | 63.7 | 3947.3 | 2.26 | 6.44 |

¹ Excess porosities and lack of penetration.

3.2. Effects of Heat Input on the Tensile Strength and Fracture Morphology of TIG (Tungsten Inert Gas) Welded Joint with Porosity Defects

As seen from Tables 2 and 4, the welding current, preheat, and interpass temperature of plates No. 1 and No. 2 were the same. The welding pool during welding was difficult to be quickly formed due to the low welding current, so the welding speed was also extremely low (approximately 1 mm/s). The TQ of plates No. 1 and No. 2 was high ($TQ > 5000$ kJ) due to the low welding speed. The fracture location occurred in the HAZ and the joint efficiency factor T was only 0.47–0.50, which indicated that serious overaging occurred in the base metal. When compared with that of plate No. 1, the TQ of plate No. 2 was lower, so the tensile strength of plate No. 2 was slightly higher. Each weld pass of plate No. 3 was shallow and narrow. The welding speed was high (approximately 3.3 mm/s), and the welding current was not high, so the calculated TQ was only 4011 kJ. The softening effect of joint No. 3 was weaker as compared with that of plates No. 1 and No. 2. The T of plate No. 3 was 0.62, which met the requirements of the standard ISO 15614-2:2005(E).

The TQ of plates No. 4 and No. 5 was in the range of 4800–4900 kJ, and the T was approximately 0.58. When compared with the data of plates No. 1 and No. 2, the TQ of plates No. 4 and No. 5 was reduced by 32%, and the tensile strength was increased by 24%. As shown in Figure 2a, porosities were found in the WZ but were not responsible for the tensile failure of plate No. 4 because the dispersive distribution of the porosities in the WZ could only reduce the effective bearing area of WZ to a limited extent, while aggregation and coarsening of Mg_2Si particles in the HAZ under high heat input condition could result in a sharp deterioration of the mechanical properties of the welded joint [6]. Thus, the fracture location of joint No. 4 was in HAZ, not in WZ. The TQ of plate No. 5 was close to that of plate No. 4, and the tensile strength and elongation of plates No. 4 and No. 5 should be close to each other by inference. However, as shown in Figure 3a, for welded joint No. 5, serious stress concentration existed at the interface between the first face weld pass and the first back weld pass. The cracks would first initiate here and then propagate rapidly along the vertical direction of the tensile stress axial line, which resulted in a sharp decline in the elongation of welded joint No. 5 and caused the failure to occur in the WZ.

The TQ of plate No. 6 was the smallest among all of the plates. Theoretically, it can be inferred that the tensile strength of plate No. 6 should be greater than or at least equal to 192 MPa according to the TQ value and tensile strength of plates No. 3, No. 7, and No. 8. However, due to the densely distributed porosities existing in the WZ (Figures 2b and 3b) and weakening of overaging in HAZ because of lower heat input, the final fracture occurred in WZ. The T of plate No. 6 was 0.62, and the elongation was 4.2%. Through the comparison of plates No. 4 and No. 6, for a TIG welded joint with porosities in the WZ and overaging in the HAZ at the same time, the tensile fracture location was uncertain. It was more likely to occur in HAZ (high heat input) and could also possibly occur in WZ (low heat input; many large porosities or high weld percent porosity). Although the welding current of plates No. 7 and plate No. 8 was over 300 A, the welding speed was high (approximately 2–2.5 mm/s), and the calculated TQ was low ($TQ < 4000$ kJ), causing the T of plate No. 7 and plate No. 8 to be in the range of 0.63–0.65.

To sum up, the various changes in the welding process parameters including the welding current, welding speed, and weld passes can be attributed to the changes of heat input during welding. Effective data concerning the heat input (including TQ and Q) and tensile strength of welded joints (except plates No. 5 and No. 6) were used to draw the following curves of Figure 4. As shown in Figure 4, a linear relationship between fracture strength $R_m(w)$ and TQ was found, while the relationship between $R_m(w)$ and Q appeared to be more complex and/or inaccurate. In addition, for a TIG welded 6082-T6 alloy with a thickness of 12 mm, controlling the TQ within 5000 kJ could ensure the tensile strength of the welded joint to meet the requirement of the standard ($T \geq 0.6$).

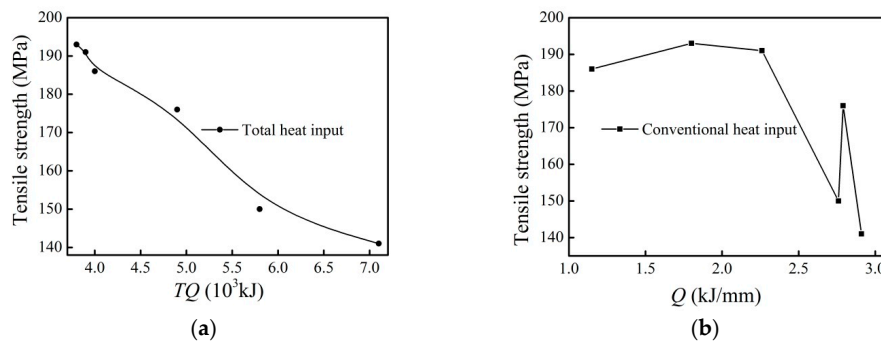


Figure 4. Effect of welding heat input on the transverse tensile strength of as-welded joints: (a) TQ (total heat input); (b) Q (heat input).

Figure 5 shows the macroscopic fracture morphologies and SEM fracture morphologies of typical as-welded specimens. As seen from Figure 5a,b, the fracture direction of specimen No. 2 was substantially perpendicular to the tension direction. The fracture morphology was a cup and cone-shaped fracture, while the fracture type of specimen No. 7 was shear fracture. The elongation of specimens No. 2 and No. 7 was high, which indicated that enough plastic deformation occurred in HAZ before the tensile fracture. The fracture mechanism was a ductile fracture, which could be explained from a microscopic point of view according to Figure 5c,d: The formation of dimples in the fracture surface implied a ductile rupture as specified in some other work [22]. The micro-fracture morphology of specimen No. 2 was equiaxed dimples, while that of tensile specimen No. 7 was shear fracture dimples. Because the types of dimples were different and the shear fracture dimples were elongated in a certain direction, the ductility of different tensile specimens cannot be evaluated by simply comparing the size and number of dimples. As seen from Figure 5e,f, many porosities with large size differences were found in the fracture morphology of tensile specimen No. 6, which badly wrecked the continuity of the microstructure of welded joint and caused the WZ to be the most dangerous area. However, many dimples were found in the SEM fracture surface at high magnification, which indicated that the fracture mechanism of plate No. 6 was also ductile fracture from the microscopic view.

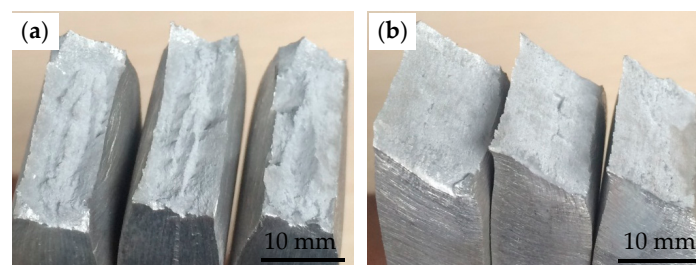


Figure 5. Cont.

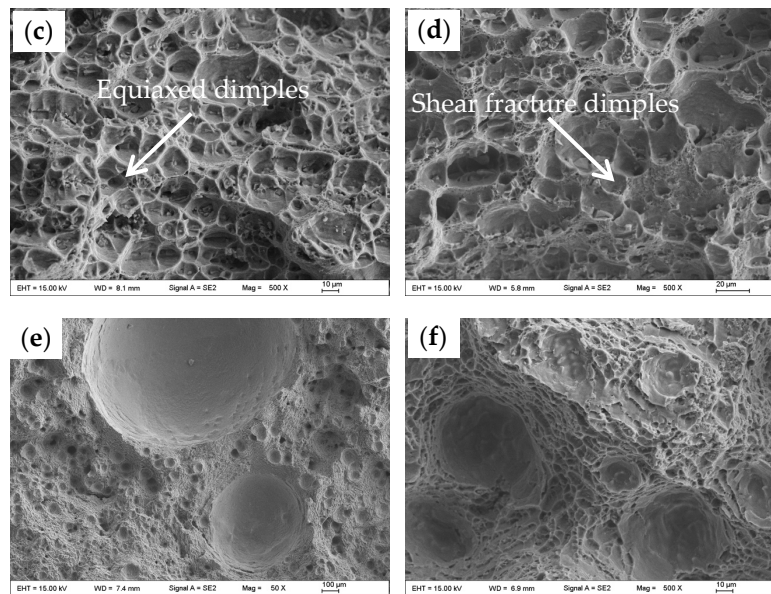


Figure 5. Macroscopic fracture morphologies of as-welded specimens: (a) sample No. 2; (b) sample No.7. SEM (scanning electron microscope) fracture morphologies of as-welded specimens: (c) sample No. 2; (d) sample No. 7; (e) sample No. 6 at low magnification; and, (f) sample No. 6 at high magnification.

3.3. Effect of Heat Input on the Microhardness and Microstructure of TIG Welded Joints

Figure 6 shows the microhardness distributions of the as-welded joints with different heat inputs during welding. It can be seen that the hardness distribution exhibited a typical “W” shape, and the minimum hardness value was located in the HAZ. This indicated that the frail position of the joints was located at the HAZ. With decreasing heat input, the minimum hardness of the HAZ increased, the distance between frail position and weld center decreased, and the average hardness of the WZ increased. At a total heat input TQ of 7126.9 kJ, the minimum hardness (40.2 HV) of the HAZ of joint No. 1 was only a third of that of the original base metal. The microhardness evolution of the welded joint can be explained by the observation and analysis of the microstructure in Figures 7–9.

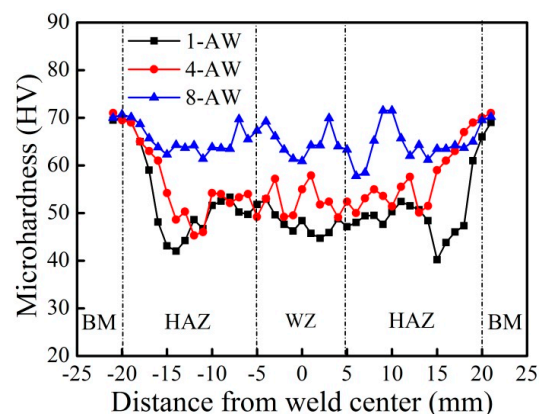


Figure 6. Microhardness distribution across the as-welded joint as a function of heat input during welding (AW: As-welded; BM: Base metal; HAZ: Heat-affected zone; WZ: Weld zone).

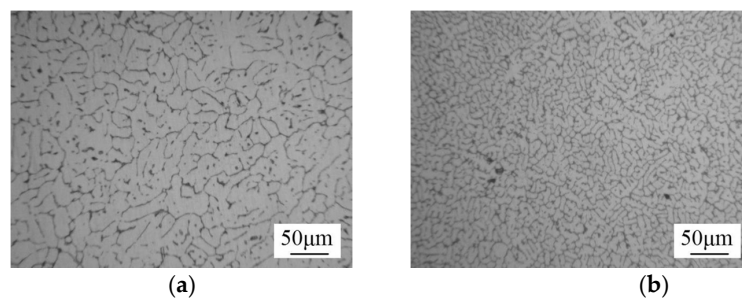


Figure 7. Microstructure of the weld center of as-welded joints under different heat inputs: (a) plate No. 1, 7126.9 kJ; (b) plate No. 8, 3947.3 kJ.

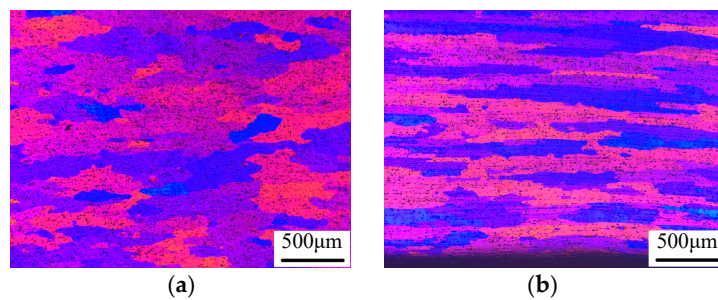


Figure 8. Microstructure of the frail position in HAZ of as-welded joints under different heat inputs: (a) plate No. 1, 7126.9 kJ; (b) plate No. 8, 3947.3 kJ.

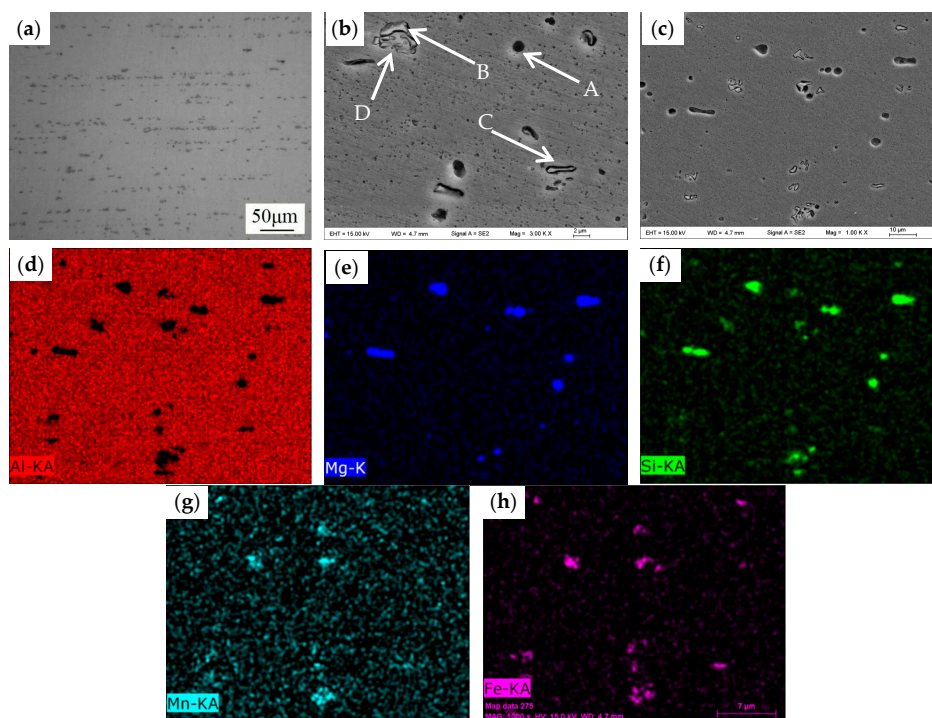


Figure 9. (a) Optical image of original 6082-T6 base metal; (b) SEM image of the frail position in HAZ of welded joint No. 7, 3784.4 kJ; SEM image and energy dispersion X-ray (EDX) maps of elements of the frail position in HAZ of welded joint No. 2, 5791.8 kJ; (c) SEM microstructure; (d) Al; (e) Mg; (f) Si; (g) Mn; (h) Fe.

Figure 7 shows the microstructure of the weld center of welded joints (without PWHT, sample No. 1 and sample No. 8). The matrix of WZ was α -Al phase, and there were many continuous network-like eutectic Si phases distributed at the grain boundaries. As observed by OM (optical microscope) in Figure 7, the average grain size of the weld center of sample No. 1 was 37.5 μm , while that of sample No. 8 was 10.6 μm , which indicated a decrease in heat input led to the refinement of the α -Al grains in the WZ, since a decrease in heat input provided less driving force for grain boundary migration that then slowed the growth of the grains [23]. Uniform and fine equiaxed grains can be found in the central area of WZ under low heat input conditions, which then enhanced the average hardness of the WZ.

The same trend in microhardness according to Figure 6 also had been found in the HAZ. Figure 8 shows the microstructure of the frail position in HAZ of as-welded joints (without PWHT, sample No. 1 and sample No. 8). As seen from the Figure 8, the grains of the HAZ were significantly elongated in the rolling direction and they were not equiaxial [24]. The average length of the grains in the rolling direction was about 741.2 μm and the average width of grains in the thickness direction of the plate No. 1 was about 257.9 μm , while the average length and the average width of the grains in the HAZ of plate No. 8 were 1255.9 μm and 107.8 μm , respectively, which indicated that the heterogeneity of the grains in HAZ of plate No. 1 was reduced more significantly due to a high heat input during the welding process. As described in the literature [25], coarse grains especially in the thickness direction were induced in the HAZ due to the weld thermal cycle. Thus, the coarse grains in HAZ under high heat input condition could be one of the reasons which resulted in the decrease of hardness in HAZ.

Figure 9 shows the SEM microstructure of original 6082-T6 base metal and the HAZ of as-welded samples. As shown in Figure 9a, a considerable amount of black precipitated phases was inhomogeneously distributed along a certain direction, which indicated that the 6082 plate was heavily rolled. Figure 9b shows the SEM image of the frail position in HAZ of welded joint No. 7. As shown in Figure 9b, the large-round black precipitated phases were partially dissolved by 0.5 wt. % HF solution and were confirmed to be the Mg_2Si phases by the EDX analysis result of Point A in Table 5. Light gray particles (Point B, C and D) were also found and contained Al, Si, Mn, and Fe, indicating that they were AlSiMnFe phases as shown in Table 5. The microstructure and EDX maps of elements of the frail position of welded joint No. 2 are shown in Figure 9c–h, which indicated that Mg and most of the element Si were distributed at the same areas and constituted the Mg_2Si phases. A small amount of element Si reacted with Mn, Fe and Al, producing the AlSiMnFe intermetallic compounds (IMCs), which were not involved in solution strengthening or precipitation strengthening. The 6082-T6 aluminum alloy is a heat-treatable alloy possessing enhanced strength due to the precipitation of Mg_2Si phase upon solution treatment and artificial aging [17]. Thus, the size and distribution of Mg_2Si phases affect the mechanical properties of the alloy. Through a comparison of Figure 9b,c, the mean sizes of the Mg_2Si phase of the frail position in HAZ of welded joints No. 7 and No. 2 were 1.80 μm and 3.36 μm , respectively. This indicated that a high heat input can induce the coarsening of Mg_2Si at the HAZ and result in a decrease of the mechanical properties of TIG welded joint. Thus, the minimum hardness of the HAZ decreased with increasing heat input.

Table 5. EDX analysis results of the points indicated in Figure 8b (wt. % or at. %).

| Point | Al | Mg | Si | Mn | Fe |
|-----------|-------|-------|-------|------|-------|
| A (at. %) | 50.22 | 33.83 | 15.95 | - | - |
| B (wt. %) | 61.27 | 0.84 | 6.45 | 9.81 | 21.63 |
| C (wt. %) | 62.16 | 1.00 | 4.08 | 4.38 | 28.37 |
| D (wt. %) | 88.63 | 0.77 | 2.50 | 2.04 | 6.06 |

3.4. Effect of PWHT on the Tensile Strength and Fracture Morphology of the TIG Welded Joints with Porosity Defects

Figure 10 shows the tensile strengths and elongations of the welded joints after different kinds of PWHTs. It can be seen that the tensile strength values of AG-joints (AG: Artificial aging treatment) No.2, No. 3, No. 7, and No. 8 were higher by 12.7%, 10.2%, 9.8%, and 10.5%, respectively, than those of the AW-joints (AW: As welded). The amplitudes of ascension were basically the same (the increments were 19–20 MPa). The elongation values of AG-joints of samples No. 2, No. 3, No. 7, and No. 8 were lower by 30.4%, 31.2%, 21.2%, and 26.8% as compared to those of AW-joints, respectively. It is already known that the mechanical properties of AW-joints decrease seriously due to the aggregation and coarsening of Mg_2Si particles under the welding thermal cycle. For the AG-joint, the fracture still occurred in the overaging area of HAZ and the frail position in HAZ cannot be changed. However, the reason for the improvement of the mechanical properties of the AG-joint is that artificial aging treatment can prompt a certain number of Mg_2Si particles with an appropriate size to precipitate in HAZ, which can reduce the overaging degree of HAZ.

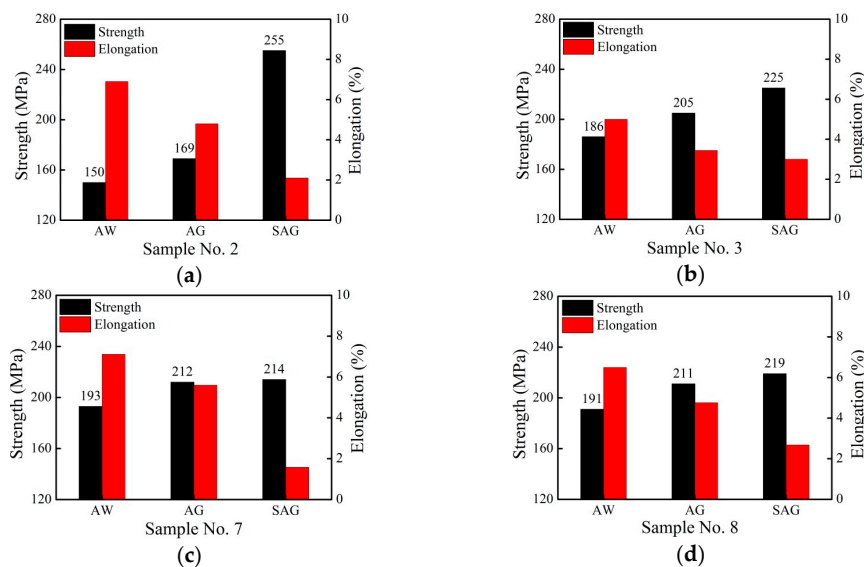


Figure 10. Effect of different PWHTs on the mechanical properties of welded joints: (a) sample No. 2; (b) sample No. 3; (c) sample No. 7; and (d) sample No. 8.

When compared with AW-joints No. 2, No. 3, No. 7, and No. 8, the tensile strength values of SAG-joints (SAG: Solution treatment + artificial aging treatment) were increased by 70%, 21.0%, 10.9%, and 14.7%, respectively. The fracture of all the SAG-joints occurred in WZ, not in HAZ. For HAZ of SAG-joint, the Mg_2Si precipitates with different sizes were all dissolved into the matrix by solution treatment and quenching in water; then, the fine Mg_2Si phases were homogeneously precipitated and the mechanical property of HAZ recovered to that of the original base metal [20]. Meanwhile, with regard to the WZ of the SAG-joint, the weld defects (porosities) could not be eliminated by the SAG process, which caused the WZ to be in a dangerous area and resulted in the fracture of WZ. In addition, it can be seen from Figure 10 that there was a huge difference in the amplitude of ascension in the tensile strength of four kinds of SAG-joints, and the elongations decreased sharply, which can be explained through Figures 11 and 12. For SAG-joints No. 2 and No. 7, a sudden stop at the rising phase of the tensile curve was found in Figure 11a,b, which showed that the SAG-joint was suddenly fractured for some reason. The yield strength and the tensile strength were the same, and the elongation was very low. As seen from the SEM fracture morphologies of SAG-joints No. 2 and No. 7 (Figure 12c–f), a large number of porosities were found throughout the weld metal, and it can be concluded that the crack initiated from the defective region and then propagated through

the weld metal. A brittle fracture surface was observed in the defective areas, followed by ductile failure behavior in the nondefective regions (Figure 12f). Porosities are usually subsurface defects and are also a source of stress concentration, but their effects are considerably lower than surface defects, such as lack of penetration (sample No. 5) [8]. For a better understanding of the effect of porosities on the mechanical properties of SAG-joint, the SEM fracture morphologies of SAG-joints No. 2 and No. 7 were compared. As expected, because the quantity and size of porosities of SAG-joint No. 2 were smaller than those of SAG-joint No. 7 (Figure 12c,d), the tensile strength, as well as the elongation of SAG-joint No. 2, was higher than that of SAG-joint No. 7. In addition, as seen from Figure 12a,b, coarse phases with a strip structure, which can be identified as Mg_2Si phases by EDS (Energy dispersive X-ray spectroscopy) analysis, were found at the bottom of the dimples, revealing that the artificial aging treatment can only produce enhancement of the mechanical properties of the welded joint to a limited extent.

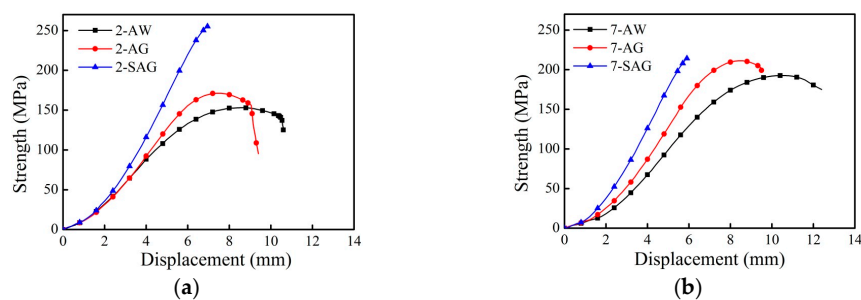


Figure 11. Tensile curves of welded joints after different kinds of PWHTs: (a) sample No. 2; (b) sample No. 7.

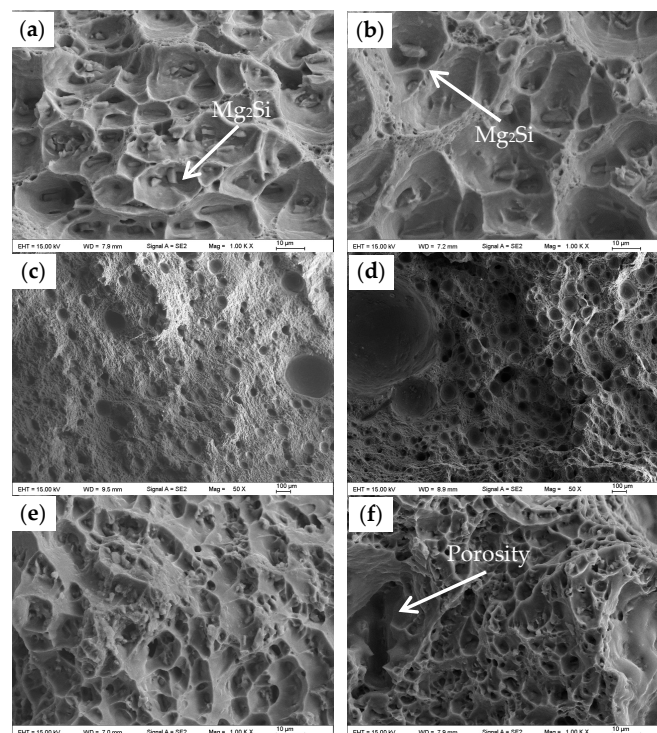


Figure 12. SEM fracture morphologies of AG-joints: (a) sample No. 2; (b) sample No. 7. SEM fracture morphologies of SAG-joints: (c) sample No. 2 at low magnification; (d) sample No. 7 at low magnification; (e) sample No. 2 at high magnification; and (f) sample No. 7 at high magnification.

3.5. Effect of PWHT on the Microhardness and Microstructure of TIG Welded Joints with Porosity Defects

The microhardness distribution curves of welded-joints No. 2 and No. 7 under three kinds of PWHTs are shown in Figure 13. For welded joints No. 2 and No. 7, the hardness of HAZ of AW-joint was low, which was due to the coarse grains and serious overaging occurring in HAZ. As compared to the AW-joints, the hardness of HAZ of AG-joint increased to a limited extent, while the hardness of HAZ of SAG-joint was restored to the level of the original 6082-T6 base metal. Therefore, it can be concluded that the AG process improved the overaging degree of HAZ, while the SAG process eliminated the softening effect of HAZ and resulted in a uniform performance of the base metal, which was achieved by prompting all strengthening phases including coarse particles to dissolve in the matrix and to re-precipitate uniformly with refined size. In addition, the hardness of the weld center of joints No. 2 and No. 7 also increased after the AG process and SAG process, as illustrated in Figure 13a,b, which can be explained through the analysis of microstructure evolution (see Figure 14) and chemical composition (see Table 6).

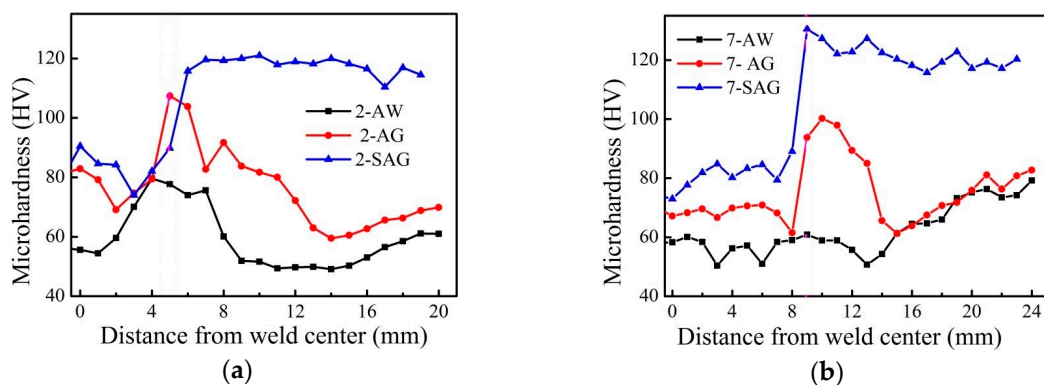


Figure 13. Microhardness distributions across the welded joints with different types of PWHTs: (a) welded joint No. 2; (b) welded joint No. 7.

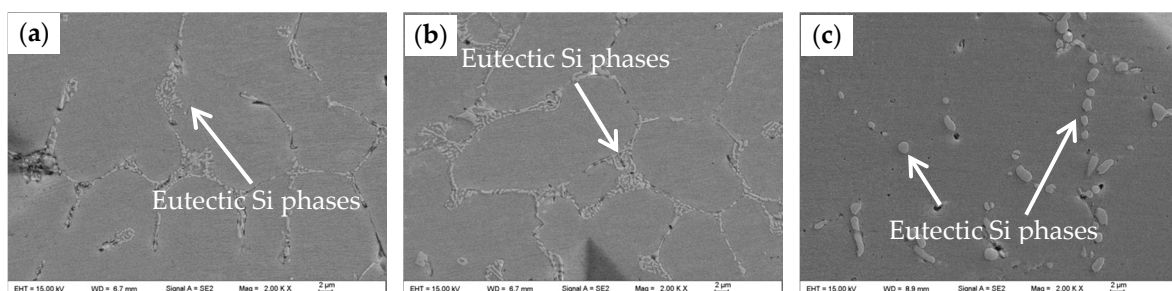


Figure 14. SEM microstructures of the weld center of welded joint No. 2 with different kinds of PWHTs: (a) AW; (b) AG; (c) SAG.

Table 6. Component analysis of a tungsten inert gas (TIG) welded joint by spectrometry (Points ①–④ seen in Figure 15).

| Point | Chemical Element Content (wt. %) | | | | | | |
|-------|----------------------------------|-------|-------|-------|------|-------|-----------|
| | Si | Fe | Cu | Mn | Mg | Ti | Al |
| ① | 2.78 | 0.195 | 0.029 | 0.296 | 0.72 | 0.018 | Remainder |
| ② | 3.15 | 0.158 | 0.022 | 0.216 | 0.54 | 0.018 | Remainder |
| ③ | 1.14 | 0.280 | 0.056 | 0.51 | 1.10 | 0.016 | Remainder |
| ④ | 0.83 | 0.281 | 0.059 | 0.55 | 1.14 | 0.018 | Remainder |

Through the comparison of the metallographic microstructures of the AW-joint, AG-joint, and SAG-joint, the grain size of the weld center of the welded joint with different kinds of PWHTs was similar to each other, which indicated that PWHT including AG and SAG had no significant influence on the grain size of the welded joints. Representative SEM microstructures of the weld center of welded joint No. 2 with different types of PWHTs are shown in Figure 14. After welding and solidification, the weld microstructures of the AW-joint appeared dendritic and owing to the temperature gradient, the edge of the weld exhibited more columnar dendrites in contrast to the equiaxed dendrites found at the center of the weld [26]. For the AW-joint and AG-joint that were welded with ER4043 filler metal, the weld center was characterized by an Al-rich matrix and secondary eutectic phases that were present as an interdendritic network. The secondary eutectic phases consisted of elements Al and Si and were determined as eutectic Si phases by EDS analysis. From the perspective of component analysis by spectrometry, the root pass and upper pass of the weld center were made up of elements Al, Si, Mg, Mn, Fe, Cu, and Ti, according to Figure 15 and Table 6 (Points ① and ② in Table 6). Thus, it can be inferred that Mg_2Si particles also existed in the weld metal, which was also confirmed by previous reports [3,27]. For the welded joint No. 2, the hardness values of the weld center of the AW-joint, AG-joint, and SAG-joint were 55.6 HV, 82.9 HV, 90.5 HV, respectively. When compared to the AW-joint, the weld center hardness of the AG-joint was higher, which can be ascribed to the precipitation of new Mg_2Si particles in WZ. Taking the effect of solution treatment on the weld metal of SAG-joint into consideration, the solid solubility of elements Si and Mg in eutectic Al-Si alloy and Al-Mg-Si alloy at high temperature was used to analyze the solution state of elements Mg and Si in WZ. For eutectic Al-12.5 wt. %Si alloy at 577 °C, the solid solubility of Si in Al was 1.65 wt. %. For Al-Mg-Si ($\omega(Si + Mg) < 2.0$ wt. %) alloy at 527 °C, the solid solubility of Si in Al near the Al corner did not exceed 0.80 wt. %, while the solid solubility of Mg in Al exceeded 0.60 wt. %. Thus, it can be inferred that after solution treatment, Mg_2Si strengthening phases of the upper pass of weld center with 3.15 wt. % Si and 0.54 wt. % Mg were all dissolved into the matrix at 530 °C, while the majority of eutectic Si phases were not dissolved into the matrix and was not then involved in precipitation strengthening. Moreover, when soaking at high temperature (530 °C), the eutectic Si phase was further adjusted into a large globular shape. In contrast with the eutectic Si morphology of the weld metal of the SAG-joint, that of AW-joint and AG-joint exhibited a fine fibrous morphology. As is known [28], solution treatment can coarsen and spheroidize the eutectic Si particles. Zhang et al. [29] reported that a solution treatment of 30 min at 540 °C or 550 °C on a Sr-modified Al-7%Si-0.3%Mg alloy caused spheroidization, coarsening and an increase in the inter-particle spacing of the eutectic silicon particles, leading to a significant improvement in ductility and impact resistance. However, it is important to note that although the rounder eutectic Si can reduce stress concentration [30], the overgrowth of the eutectic Si particles, which is aroused by soaking at high temperature and implemented by diffusion of Si to the surface of the original Si phases, will reduce the toughness of the weld metal. The increase of the hardness of weld metal of the SAG-joint as compared to AG-joint can be explained by the following reasons: (1) Homogeneity and maximum solubility of the alloy elements in the matrix were obtained during the solution treatment. It can be deduced that although not observed, a large number of small Mg_2Si particles uniformly precipitated from the solid solution during the artificial aging treatment, thus improving the hardness. (2) Although the coarsening of the eutectic Si phase caused by the solution treatment resulted in a drop of hardness, the spheroidization of eutectic Si phase can increase the hardness. Based on the above analysis, it can be concluded that the combined positive effect of precipitation strengthening of Mg_2Si and the spheroidization of eutectic Si phase on the hardness was stronger than the negative effect of the coarsening of the eutectic Si phase.

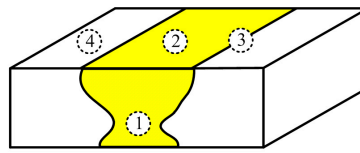


Figure 15. Schematic diagram of characteristic points of a welded joint for component analysis: ① root pass of the weld center; ② upper pass of the weld center; ③ boundary between the WZ and the HAZ; ④ HAZ.

4. Conclusions

The effects of heat input and post-weld heat treatment on the microstructure evolution and mechanical properties of TIG welded joints of AA6082-T6 containing porosity defects were successfully investigated. The conclusions are as follows:

- (1) For a TIG welded joint of 6082-T6 with porosities in the WZ and overaging in the HAZ at the same time, the tensile fracture location was uncertain. Fracture was more likely to occur in HAZ (high heat input), and possibly occurred in WZ (low heat input; many large porosities or high weld percent porosity).
- (2) When the fracture occurred in HAZ, the total heat input TQ had a linear relation with the tensile strength of the as-welded joint. High heat input during welding can induce the overgrowth of Mg_2Si precipitates in HAZ and the coarsening of $\alpha-Al$ grains in WZ, resulting in a decrease in the microhardness of the corresponding areas.
- (3) The tensile strength of the welded joint increased by approximately 9–13% after the artificial aging treatment as compared to that of the as-welded joint, and the fracture location was also located in HAZ. For the SAG-joint, the tensile strength was the same as the yield strength, and the fracture occurred suddenly at the rising phase of the tensile curve due to porosity defects throughout the weld metal.
- (4) No appreciable changes in the weld metal microstructure of the welded joint were noticed after the artificial aging treatment, while the eutectic Si particle of the weld metal coarsened and spheroidized after the SAG process, which resulted from the diffusion of Si to the surface of the original Si phases when soaking at high temperature.

Acknowledgments: This work is financially supported by the National Natural Science Foundation of China (Grant No. 51375233, 51305173), China Postdoctoral Science Foundation (General Financial Grant No. 2014M550289, Special Financial Grant No. 2015T80548), and the Priority Academic Program Development of Jiangsu Higher Education Institutions (PAPD).

Author Contributions: Bo Wang, Songbai Xue and Jianxin Wang conceived and designed the experiments; Bo Wang and Chaoli Ma performed the experiments; Bo Wang and Songbai Xue analyzed the data; Zhongqiang Lin contributed reagents/materials/analysis tools; Bo Wang wrote the paper.

Conflicts of Interest: The authors declare no conflict of interest.

References

1. Fahimpour, V.; Sadrnezhad, S.K.; Karimzadeh, F. Corrosion behavior of aluminum 6061 alloy joined by friction stir welding and gas tungsten arc welding methods. *Mater. Des.* **2012**, *39*, 329–333. [[CrossRef](#)]
2. Imam, M.; Racherla, V.; Biswas, K. Effect of post-weld natural aging on mechanical and microstructural properties of friction stir welded 6063-T4 aluminium alloy. *Mater. Des.* **2014**, *64*, 675–686. [[CrossRef](#)]
3. Chen, Q.; Ge, H.; Yang, C.; Lin, S.; Fan, C. Study on pores in ultrasonic-assisted TIG weld of aluminum alloy. *Metals* **2017**, *7*, 53. [[CrossRef](#)]
4. Liang, Y.; Hu, S.S.; Shen, J.Q.; Zhang, H.; Wang, P. Geometrical and microstructural characteristics of the TIG-CMT hybrid welding in 6061 aluminum alloy cladding. *J. Mater. Process. Technol.* **2017**, *239*, 18–30. [[CrossRef](#)]

5. Narsimhachary, D.; Bathe, R.N.; Padmanabham, G.; Basu, A. Influence of temperature profile during laser welding of aluminum alloy 6061 T6 on microstructure and mechanical properties. *Mater. Manuf. Process.* **2014**, *29*, 948–953. [[CrossRef](#)]
6. Wang, Q.; Chen, H.; Zhu, Z.; Qiu, P.; Cui, Y. A characterization of microstructure and mechanical properties of A6N01S-T5 aluminum alloy hybrid fiber laser-MIG welded joint. *Int. J. Adv. Manuf. Technol.* **2016**, *86*, 1375–1384. [[CrossRef](#)]
7. Ambriz, R.R.; Chicot, D.; Benseddiq, N.; Mesmacque, G.; de la Torre, S.D. Local mechanical properties of the 6061-T6 aluminium weld using micro-traction and instrumented indentation. *Eur. J. Mech. A* **2011**, *30*, 307–315. [[CrossRef](#)]
8. Dewan, M.W.; Wahab, M.A.; Okeil, A.M. Influence of weld defects and postweld heat treatment of gas tungsten arc-welded AA-6061-T651 aluminum alloy. *J. Manuf. Sci. Eng.* **2015**, *137*, 051027. [[CrossRef](#)]
9. Attar, H.; Bönisch, M.; Calin, M.; Zhang, L.C.; Scudino, S.; Eckert, J. Selective laser melting of in situ titanium-titanium boride composites: Processing, microstructure and mechanical properties. *Acta Mater.* **2014**, *76*, 13–22. [[CrossRef](#)]
10. Attar, H.; Ehtemam-Haghighi, S.; Kent, D.; Wu, X.H.; Dargusch, M.S. Comparative study of commercially pure titanium produced by laser engineered net shaping, selective laser melting and casting processes. *Mater. Sci. Eng. A* **2017**, *705*, 385–393. [[CrossRef](#)]
11. Rudy, J.F.; Rupert, E.J. Effects of porosity on mechanical properties of aluminum welds. *Weld. J.* **1970**, *49*, 322–336.
12. Gou, G.; Zhang, M.; Chen, H.; Chen, J.; Li, P.; Yang, Y.P. Effect of humidity on porosity, microstructure, and fatigue strength of A7N01S-T5 aluminum alloy welded joints in high-speed trains. *Mater. Des.* **2015**, *85*, 309–317. [[CrossRef](#)]
13. Morton, T.M. Defects in 2021 aluminum alloy welds. *Weld. J.* **1971**, *50*, 304–312.
14. Malin, V. Study of metallurgical phenomena in the HAZ of 6061-T6 aluminum welded joints. *Weld. J.* **1995**, *74*, 305–318.
15. Lin, Y.T.; Wang, D.P.; Wang, M.C.; Zhang, Y.; He, Y.Z. Effect of different pre-and post-weld heat treatments on microstructures and mechanical properties of variable polarity TIG welded AA2219 joints. *Sci. Technol. Weld. Join.* **2016**, *21*, 234–241. [[CrossRef](#)]
16. Menzemer, C.; Hilty, E.; Morrison, S.; Minor, R.; Srivatsan, T. Influence of post weld heat treatment on strength of three aluminum alloys used in light poles. *Metals* **2016**, *6*, 52. [[CrossRef](#)]
17. Huang, Y.X.; Wan, L.; Lv, Z.L.; Lv, S.X.; Zhou, L.; Feng, J.C. Microstructure and microhardness of aluminium alloy friction stir welds with heat treatment. *Sci. Technol. Weld. Join.* **2016**, *21*, 637–644. [[CrossRef](#)]
18. Zhu, Z.Y.; Deng, C.Y.; Wang, Y.; Yang, Z.W.; Ding, J.K.; Wang, D.P. Effect of post weld heat treatment on the microstructure and corrosion behavior of AA2219 aluminum alloy joints welded by variable polarity tungsten inert gas welding. *Mater. Des.* **2015**, *65*, 1075–1082. [[CrossRef](#)]
19. Balasubramanian, V.; Ravisankar, V.; Reddy, G.M. Effect of pulsed current and post weld aging treatment on tensile properties of argon arc welded high strength aluminium alloy. *Mater. Sci. Eng. A* **2007**, *459*, 19–34. [[CrossRef](#)]
20. Pérez, J.S.; Ambriz, R.R.; López, F.F.C.; Viguera, D.J. Recovery of mechanical properties of a 6061-T6 aluminum weld by heat treatment after welding. *Metall. Mater. Trans. A* **2016**, *47*, 3412–3422. [[CrossRef](#)]
21. Zhang, C.; Gao, M.; Wang, D.Z.; Yin, J.; Zeng, X.Y. Relationship between pool characteristic and weld porosity in laser arc hybrid welding of AA6082 aluminum alloy. *J. Mater. Process. Technol.* **2017**, *240*, 217–222. [[CrossRef](#)]
22. Ehtemam-Haghighi, S.; Liu, Y.J.; Cao, G.H.; Zhang, L.C. Phase transition, microstructural evolution and mechanical properties of Ti-Nb-Fe alloys induced by Fe addition. *Mater. Des.* **2016**, *97*, 279–286. [[CrossRef](#)]
23. Min, D.; Shen, J.; Lai, S.Q.; Chen, J. Effect of heat input on the microstructure and mechanical properties of tungsten inert gas arc butt-welded AZ61 magnesium alloy plates. *Mater. Charact.* **2009**, *60*, 1583–1590. [[CrossRef](#)]
24. Sillapasa, K.; Surapunt, S.; Miyashita, Y.; Mutoh, Y.; Seo, N. Tensile and fatigue behavior of SZ, HAZ and BM in friction stir welded joint of rolled 6N01 aluminum alloy plate. *Int. J. Fatigue* **2014**, *63*, 162–170. [[CrossRef](#)]
25. Shen, Z.K.; Yang, X.Q.; Yang, S.; Zhang, Z.H.; Yin, Y.H. Microstructure and mechanical properties of friction spot welded 6061-T4 aluminum alloy. *Mater. Des.* **2014**, *54*, 766–778. [[CrossRef](#)]

26. Elrefaey, A.; Ross, N.G. Microstructure and mechanical properties of cold metal transfer welding similar and dissimilar aluminum alloys. *Acta Metall. Sin.* **2015**, *28*, 715–724. [[CrossRef](#)]
27. Sevim, I.; Hayat, F.; Kaya, Y.; Kahraman, N.; Şahin, S. The study of MIG weldability of heat-treated aluminum alloys. *Int. J. Adv. Manuf. Technol.* **2013**, *66*, 1825–1834. [[CrossRef](#)]
28. Forn, A.; Baile, M.T.; Martín, E.; Rupérez, E. Effect of heat treatments in the silicon eutectic crystal evolution in Al-Si alloys. *Mater. Sci. Forum* **2005**, *480–481*, 367–372. [[CrossRef](#)]
29. Zhang, D.L.; Zheng, L.H.; StJohn, D.H. Effect of a short solution treatment time on microstructure and mechanical properties of modified Al-7 wt. %Si-0.3 wt. %Mg alloy. *J. Light Met.* **2002**, *2*, 27–36. [[CrossRef](#)]
30. Yang, Y.; Zhong, S.Y.; Chen, Z.; Wang, M.; Ma, N.; Wang, H. Effect of Cr content and heat-treatment on the high temperature strength of eutectic Al-Si alloys. *J. Alloys Compd.* **2015**, *647*, 63–69. [[CrossRef](#)]



© 2017 by the authors. Licensee MDPI, Basel, Switzerland. This article is an open access article distributed under the terms and conditions of the Creative Commons Attribution (CC BY) license (<http://creativecommons.org/licenses/by/4.0/>).